Journal of Alloys and Compounds 621 (2015) 104–115

Contents lists available at ScienceDirect

Journal of Alloys and Compounds

journal homepage: www.elsevier.com/locate/jalcom

Effects of Nd on the properties of CeO_2–ZrO_2 and catalytic activities of three-way catalysts with low Pt and Rh

Jiaxiu Guo [a,c,d,*], Zhonghua Shi [b,d], Dongdong Wu [b], Huaqiang Yin [a,c,d], Maochu Gong [b], Yaoqiang Chen [b,c,d,*]

[a] College of Architecture and Environment, Sichuan University, Chengdu 610065, China
[b] College of Chemistry, Sichuan University, Chengdu 610064, China
[c] National Engineering Research Center for Flue Gas Desulfurization, Chengdu 610065, China
[d] Sichuan Provincial Environmental Protection Environmental Catalysis and Materials Engineering Technology Center, Chengdu 610065, China

ARTICLE INFO

Article history:
Received 4 July 2014
Received in revised form 12 September 2014
Accepted 24 September 2014
Available online 2 October 2014

Keywords:
Ceria
Three-way catalyst
Platinum
Neodymium
Sintering

ABSTRACT

A series of $Ce_{0.35}Zr_{0.65-x}Nd_xO_{2-x/2}$ (x = 0.05, 0.10, 0.15, 0.20 and 0.25) were prepared, and the combinational effects of Nd and noble metals on the catalytic activities of monolithic cordierite honeycomb catalysts were elucidated. The results showed that the BET surface area and pore volume of CZN3F reach a maximum, 97 m^2/g and 0.19 ml/g, but all aged samples undergo a sharp decline. The CZN2 has more oxygen vacancy and higher oxygen storage capacity (OSC) before and after ageing, but OSC of the samples with high Nd content decreases. All fresh samples have cubic $Ce_{0.40}Zr_{0.60}O_2$ phase with nano-size, but the aged samples with low Nd content still exhibit cubic $Ce_{0.40}Zr_{0.60}O_2$ phase. When Nd content (CZN4A) is 20 mol% after ageing at 1000 °C, small $Ce_{0.60}Nd_{0.40}O_{1.80}$ is segregated from CeO_2–ZrO_2 cubic phase; when the doped Nd increases to 25 mol% (CZN5A), the CeO_2–ZrO_2 cubic phase completely converts into $Nd_{050}Zr_{0.50}O_{1.75}$ cubic phase with 12.4 nm, accompanying a sharp decline of OSC; and O_2 pretreatment can change the reductive behavior and H_2 consumption of samples because of oxygen absorbed. Noble metals can influence the reduction of $Ce_{0.35}Zr_{0.65-x}Nd_xO_{2-x/2}$. $Ce_{0.35}Zr_{0.65-x}Nd_xO_{2-x/2}$ shows important differences in the TPR and H_2 consumption and can change the dispersion and sintering of noble metals, resulting in different catalytic activities. The light-off temperature ($T_{50\%}$) of catalysts containing CZN2F (C2F) can be as low as 160 °C for CO, 211 °C for NO and 259 °C for C_3H_8, indicating that appropriate Nd doping is helpful for the improving catalytic activity.

1. Introduction

Since the end of last century, in order to solve the problems of cold start and increasingly tight supply of precious metals, a new study is focused on the development of Pd-only or Pt and Rh three-way catalysts (TWCs) with low content. According to the literature [1], the total precious metals of Pt and Rh (Pt:Rh = 5:1) in TWCs have been dropped to 0.30–1.2 g/L, and the conversion of CO, HC and NO_x can still meet the automobile emission regulations. The study by Huang et al. [2] indicates that the TWCs with high rare earth oxides have high conversion of CO, HC and NO_x when the precious metals decrease to 0.35–0.564 g/L.

Generally, a conventional TWC involve two main carriers: oxygen storage materials such as CeO_2 and CeO_2–ZrO_2 and carriers with high surface area and anti-sintering at high temperature such as Al_2O_3 and La_2O_3-stabilized Al_2O_3. Catalyst deactivation may be caused by a number of reasons, both chemical and physical. Although the introduction of CeO_2–ZrO_2-based mixed oxides into the TWCs represents a significant breakthrough point compared to the CeO_2-based technology, as rougher working condition of TWCs and more rigorous emission regulations applied, better performance and thermal stable CeO_2-based material is required for developing durable and versatile TWC converters with high-activities. A successful commercial TWC application must meet the requirements of high thermal stability and activity, especially 1000 °C.

In principle, there are a number of routes to improve the oxygen storage capacity (OSC) and thermal stability of CeO_2–ZrO_2-based materials. It is reported that the highest OSC is shown by $Ce_{1-x}Zr_xO_{2-x}$ with x = 0.2–0.4 [3], whereas lower CeO_2 content

* Corresponding authors. Address: College of Architecture and Environment, Sichuan University, Chengdu 610065, China. Tel./fax: +86 28 85403016 (J. Guo). Address: College of Chemistry, Sichuan University, Chengdu 610064, China. Tel./fax: +86 28 85418451 (Y. Chen).
E-mail addresses: guojiaxiu@scu.edu.cn (J. Guo), chenyaoqiang@scu.edu.cn (Y. Chen).

http://dx.doi.org/10.1016/j.jallcom.2014.09.189
0925-8388/

favors highest textural stability under equivalent synthesis conditions [4]. Nevertheless, the complete control of the design and synthesis of these systems is still quite far from being achieved, because the crystal structure of a CeO_2–ZrO_2 depends on chemical composition and synthesis procedure. In our previous studies [5], Nd doping into CeO_2–ZrO_2 can improve the catalytic activities of TWCs. Wang et al. [6] studied the effect of Nd doping on the properties of CeO_2–ZrO_2 solid solutions and the catalytic performance of its supported Pd-only TWCs for gasoline engine exhaust. They demonstrated that the addition of Nd is resultant in the formation of cerium–zirconium–neodymium ternary oxide solid solution with better textural and structural properties than a similar undoped ceria–zirconia mixed oxide, as well as the improved reducibility and redox behavior, leading to the enhancement of three-way catalytic activity and enlargement of air/fuel operation window. However, the effects of Nd with different doping content on the TWCs with low Pt and Rh are not systematically studied. In fact, the catalytic properties of a material depend not only on the chemical nature of the components and their ratio but also on the particles dimension and their nano-or micro morphology, and all of these are strongly influenced by the preparation method [7]. In this paper, CeO_2–ZrO_2 materials with different Nd content were prepared by an oxidation-co-precipitation technique and these mixed oxides were used to prepare monolithic cordierite honeycomb TWCs with low Pt and Rh of 0.50 g/L. And, the physicochemical and structural characterization of the prepared samples is carried out using X-ray diffraction (XRD), Brunauer–Emmett–Teller (BET), Raman spectroscopy and other techniques.

2. Experimental

2.1. $Ce_{0.35}Zr_{0.65-x}Nd_xO_{2-x/2}$ and catalyst preparation

According to the literature [8], $Ce_{0.35}Zr_{0.65-x}Nd_xO_{2-x/2}$ (x = 0.05, 0.10, 0.15, 0.20 and 0.25; named as CZN1, CZN2, CZN3, CZN4 and CZN5, respectively) were prepared by oxidation-co-precipitation method from the following chemicals: $Ce(NO_3)_3{\cdot}6H_2O$; $Zr(NO_3)_3{\cdot}5H_2O$; and $Nd(NO_3)_3{\cdot}6H_2O$, at the nominal composition, and the prepared $Ce_{0.35}Zr_{0.65-x}Nd_xO_{2-x/2}$ was calcined from room temperature to 600 °C with heating rate of 10 °C/min in a muffle furnace and maintained at 600 °C for 5 h under air atmosphere. These samples were calcined at 1000 °C for 5 h under air atmosphere, respectively, to compare their thermal stabilities. These samples calcined at 600 °C were named as CZN1F, CZN2F, CZN3F, CZN4F and CZN5F, respectively, and these samples calcined at 1000 °C were respectively labeled as CZN1A, CZN2A, CZN3A, CZN4A and CZN5A. The 3 wt.% La_2O_3-stabilized Al_2O_3 was prepared by the method of incipient wetness impregnation and calcined at 1000 °C in a muffle furnace under air atmosphere for 5 h to be stabilized. The heating rate is 10 °C/min. The obtained 3 wt.% La_2O_3-stabilized Al_2O_3 was named as LA and had BET surface area of 114 m^2/g and γ-Al_2O_3 phase.

The prepared $Ce_{0.35}Zr_{0.65-x}Nd_xO_{2-x/2}$ (CZN1F, CZN2F, CZN3F, CZN4F and CZN5F, respectively) and LA were used to prepare three-way catalysts with a 0.40 wt.% of Pt and Rh (Pt:Rh = 9:1). For example, the Pt and Rh-loaded CZN1F and LA catalyst powders were prepared by incipient wetness impregnation. According to a certain proportion, $RhCl_3$ and H_2PtCl_6 aqueous solutions were respectively loaded on CZN1F powders and dried at 105 °C overnight in drying oven and calcined at 550 °C for 3 h in a muffle furnace under air atmosphere. At the same time, $RhCl_3$ and H_2PtCl_6 were respectively loaded on LA and dried at 105 °C overnight in drying oven and calcined at 550 °C for 3 h in a muffle furnace under air atmosphere. The heating rate is 10 °C/min. These catalyst powders were mixed with trace amounts of necessary inorganic additives, added with some distilled water, and ball-milled to obtain homogeneous slurry. The obtained slurry was spread on a honeycomb cordierite (2.5 cm^3, Corning, Shanghai) and the excess was blown away using compressed air. This process was repeated several times to achieve a Pt and Rh loading of 0.50 g/L. The coated honeycomb cordierite was dried at 105 °C for 4 h in drying oven and calcined at 550 °C for 3 h in a muffle furnace under air atmosphere. The heating rate is 10 °C/min. Finally, a monolithic catalyst was obtained and denoted as C1F. According to the preparation method and treatment condition of C1F, CZN1F was replaced by CZN2F, CZN3F, CZN4F or CZN5F to prepare the monolithic catalysts. They were named as C2F, C3F, C4F and C5F, respectively. These fresh catalysts were hydrothermal aging at 1000 °C for 10 h in a tube furnace under 10%H_2O–90%N_2 atmosphere with 20 ml/min flow, and aged catalysts were obtained and named as C1A, C2A, C3A, C4A and C5A, respectively.

2.2. Catalytic activity evaluation

The three-way catalytic activity was evaluated in a fixed bed micro-reactor (14 mm inner diameter) with a gas mixture which simulated the exhaust from a gasoline engine. These gases were controlled using mass flow controllers before entering the blender. The gas space velocity (SV) was 34,000 h^{-1}. A λ value of 1.0 was utilized in all activity measurements. The λ-value of the simulated exhaust represents the ratio of available to needed oxygen for a complete conversion of the components to CO_2, H_2O and N_2. The λ-value is defined as oxidants/reductants factor $\lambda = (2O_2 + NO)/(10C_3H_8 + CO)$. The CO, C_3H_8 and NO contents in the stimulated gas before and after the micro-reactor were analyzed on-line using a FGA-4100 five-component analyzer (Analysis Instrument Co., Ltd., Fushan). The curves about the relationship between conversion and temperature/λ were obtained. The stoichiometric simulated exhaust contained adjustable O_2, 0.646% CO, 0.081% C_3H_8, 0.10% NO, 12% CO_2, 10% H_2O and N_2 as the balance.

The conversion of CO, C_3H_8 and NO was calculated using the following formula:

$$\text{Conversion } (\%) = \frac{C_{in} - C_{out}}{C_{in}} \times 100\%$$

where C_{in} is the component concentration in the original simulated mixture before the micro-reactor, and C_{out} is the concentration after the micro-reactor.

2.3. Characterization

The N_2 adsorption isotherms of the samples at liquid nitrogen temperature were obtained on a ZXF-06 automatic surface analyzer (Xibei Chemical Institute, Xianyang, China). Samples were degassed at 350 °C for 2 h in a vacuum to desorb surface impurities. The adsorption isotherm data were used to calculate the surface area (S_{BET}) of each sample using the Brunauer–Emmett–Teller (BET) equation at relative pressures between 0.05 and 0.35.

Laser Raman spectra were recorded using a LabRAM HR Raman spectrometer (HORIBA Jobin Yvon Co., Paris, France) with a 30 mW Ar ion laser (532 nm). The crystal structures of all samples were determined using an X-ray diffractometer (XRD) (DX-2000; Dandong Fangyuan Instrument Co., China) with Cu Kα radiation (λ = 0.15406 nm). The X-ray tube was operated at 40 kV and 25 mA. The samples were scanned within the 2θ range of 10–90° at a scanning rate of 0.03 deg/s. The crystalline phases were identified by comparing them with reference data from the International Center for Diffraction Data (JCPDs). The lattice constants were calculated from peak locations and Miller indices. Particle size calculations were performed using Debye–Scherrer equation.

The 200 mg sample was reduced from room temperature (RT) to 550 °C in pure H_2 with 40 ml/min flow rate before the oxygen storage capacity (OSC) measurement. The heating rate is 10 °C/min. The sample was then maintained at this temperature for 45 min, cooled to 200 °C, and purged with pure N_2 with 20 ml/min flow rate. OSC was measured by injecting oxygen pulses (82 μmol of O_2 per g of sample) into the sample bed until no more oxygen consumption was detected by the thermal conductivity detector (TCD).

The temperature-programmed reduction of H_2 (H_2-TPR) experiments were performed in a quartz tubular micro-reactor to study the reductive performance of $Ce_{0.35}Zr_{0.65-x}Nd_xO_{2-x/2}$ pretreated by different atmosphere, including N_2 and 10%O_2–90%N_2. The 100 mg sample was pretreated under a N_2 with 20 ml/min flow rate from RT to 400 °C before the H_2-TPR measurements, maintained at this temperature for 40 min, and then cooled to RT. Another way is that 100 g sample was pretreated under a 10%O_2–90%N_2 (V/V) with 20 ml/min flow rate from RT to 400 °C before the H_2-TPR measurements, maintained at this temperature for 40 min, and then cooled to RT. The H_2 uptake amount during the reduction reaction was detected using a TCD. CuO was used as a standard. The reduction reaction was performed using a 5%H_2–95%N_2 (V/V) mixture at a heating rate of 10 °C/min from RT to 800 °C.

For the catalysts, the 100 mg sample was pretreated under a N_2 with 20 ml/min flow rate from RT to 400 °C before the H_2-TPR measurements, maintained at this temperature for 40 min, and then cooled to RT. The reduction reaction was performed using a 5%H_2–95%N_2 (V/V) mixture at a heating rate of 10 °C/min from RT to 700 °C. After the first TPR, the sample was cooled to RT in a N_2 atmosphere, and the reduction reaction was started again to study the changes of reductive performance after the catalyst undergone a reduction experience. The TPR-redox cycle of catalyst was repeated two times.

The temperature-programmed desorption of NO (NO-TPD) was conducted in a quartz tubular micro-reactor to study the adsorption behavior of NO on catalysts. The 100 mg sample was initially pretreated in pure Ar with flow rate of 20 ml/min at 400 °C for 60 min before performing a NO-TPD experiment. The sample was then cooled to RT and switched to a 10%NO–90%Ar (V/V) mixture with flow rate of 20 ml/min for 90 min. The sample was heated from RT to 900 °C at a rate of 10 °C/min in pure Ar with flow rate of 20 ml/min for NO_x desorption. The effluent gas was monitored on-line using a TCD.

CO chemisorption was used to determine noble metal dispersion (Pt and Rh) on the catalyst surface. The 100 mg sample was reduced using pure H_2 with flow rate of 20 ml/min in a quartz U-tube at 550 °C for 60 min before the analysis. The samples was then purged with pure N_2 with flow rate of 20 ml/min and cooled to 25 °C. Next, the pulses of CO were injected to achieve a breakthrough point. The

dispersion of noble metals was evaluated from the consumption of CO (assuming CO/M = 1) because CO adsorption at room temperature does not change the oxidation state of the support (prereduced by hydrogen) and the composition of CeO_2–ZrO_2 seems to have no definite influence on the dispersion due to the same dispersion (60–65%) for a wide range of composition of the mixed oxide, between $Ce_{0.15}Zr_{0.85}$ and $Ce_{0.68}Zr_{0.32}$ [9].

3. Results and discussion

3.1. Structure of $Ce_{0.35}Zr_{0.65-x}Nd_xO_{2-x/2}$

XRD patterns of all samples are shown in Fig. 1. This figure gives an evidence of the existence of nano-size diffracting entities. According to the literature [10], the diffraction peaks of CeO_2 with cubic phase are 28.55°, 33.08°, 47.48°, 56.34°, 59.09°, 69.42°, 76.71° and 79.08° (JCPDs No. 43-1002). Diffraction peaks with 2θ value of 30.40°, 34.92°, 35.34°, 59.70°, 60.26°, 60.04° and 74.62° originate from the crystal planes (011), (002), (110), (013), (121), (202) and (220) of tetragonal ZrO_2 (JCPDs No. 50-1089), respectively [11]. Nd_2O_3 has two structure, body-centered cubic structure (JCPDs No. 21-0579) and hexagonal phase (JCPDs No. 41-1089) [12,13]. For CZN1F, the obvious peaks at $2\theta = 29.20°$, 33.91°, 48.97°, 58.24°, 59.77°, 72.16°, 79.51° and 81.85° can be observed. They correspond to face-centered cubic structures of CeO_2. All other samples calcined at 600 °C show a face-center cubic structure, and no evidence of the presence of other phases (m, t, t′, ZrO_2 or Nd_2O_3) is detected. This indicates that the introduction of

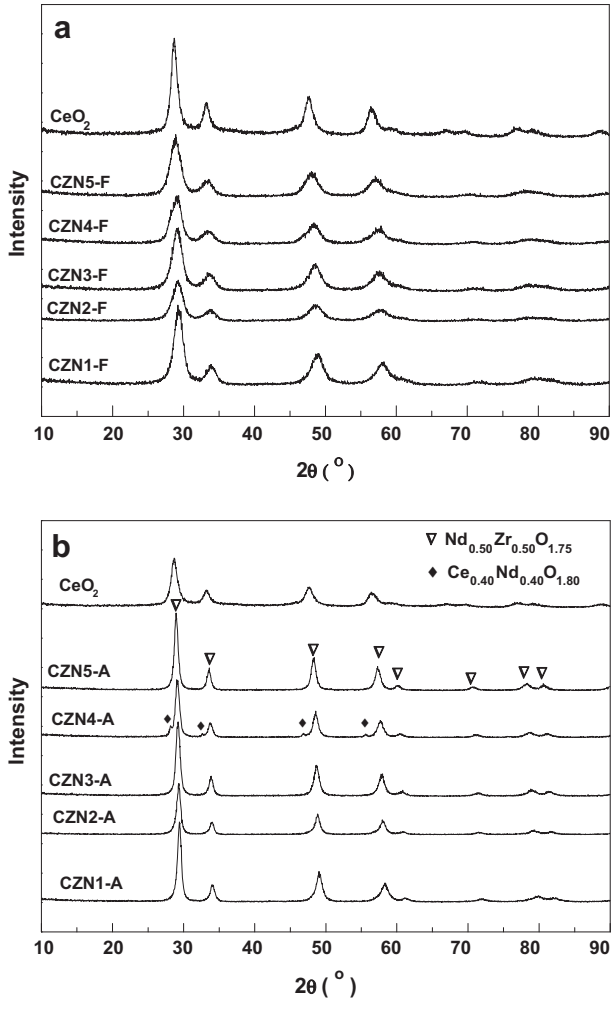

Fig. 1. XRD profile of $Ce_{0.35}Zr_{0.65-x}Nd_xO_{2-x/2}$ calcined at 600 (a) and 1000 °C (b).

Nd_2O_3 cannot change the crystalline structure of CeO_2–ZrO_2 and forms a solid solution. In other words, all Nd^{3+} ions could be dissolved into the CeO_2–ZrO_2 lattice. With the increase of Nd doping content, the diffraction angle shifts to lower angle, indicating that the lattice parameters of samples increase gradually. It is confirmed by the data in Table 1. This increase of the lattice parameter from 0.52667 nm for CZN1F to 0.53557 nm for CZN5F can be attributed to the substitution of Nd^{3+} ion at the site originally occupied by the Ce^{4+} ions. This is resultant in lattice expansion when the ion with larger radius enters into a lattice with smaller ion, because the ionic radius of Nd^{3+} (0.115 nm) is greater than that of Ce^{4+} (0.097 nm) and of Zr^{4+} (0.084 nm). A consistent peak broadening is observed, reflecting the occurrence of more defective ceria lattice, lower degree of crystallinity and smaller particle size. This defect can be explained by lattice strain. According to the results calculated by the Debye–Scherrer equation ($D = \kappa\lambda/(\beta\cos\theta)$) analyzing the half-band width (Table 1), all samples are nanocrystalline with 5.1 nm for CZN1F and 4.3 nm for CZN5F, indicating that the different Nd doping content can influence the crystalline size. The Nd doping is conducive to the production of small crystalline, which will help the improvement of the catalytic activities.

In our experimental conditions, after being aged at 1000 °C for 5 h, the diffraction peaks of all samples (Fig. 1b) become sharp, which implies the sample sintering. With the increase of Nd doping content, the diffraction angle still moves to the lower angle. When Nd content is less than 20 mol% (CZN1A, CZN2A and CZN3A), the samples are still a stable solid solution with CeO_2–ZrO_2 cubic phase; and with the increase of Nd doping content, the unit cell parameters of all samples calcined at 1000 °C increase but are smaller than the corresponding fresh samples, as shown in Table 1. This is caused by Nd^{3+} (0.115 nm) with larger ionic radius entering into the oxide lattice of Ce^{4+} (0.097 nm) with small ionic radius. For CZN4A, small $Ce_{0.60}Nd_{0.40}O_{1.80}$ (2θ at 28.15°, 33.73°, 46.69° and 55.60°) cubic phase is separated from CeO_2–ZrO_2 cubic phase, and more $Ce_{0.40}Zr_{0.60}O_2$ (JPCDs No. 38-1439) cubic phase exists in the sample. These results indicate that CZN4A appears phase separation after calcination at high temperature. For CZN5A, the diffraction peaks at 28.93°, 33.61°, 48.37°, 57.28°, 59.86°, 70.57°, 78.34° and 80.70° are observed, which conform to the XRD pattern of cubic $Nd_{0.50}Zr_{0.50}O_{1.75}$ (No. 63-6817) while deviate from the CeO_2-containing compounds, indicating that CeO_2–ZrO_2 cubic phase is completely converted into $Nd_{0.50}Zr_{0.50}O_{1.75}$ because of the rearrangement of Ce^{4+}, Nd^{3+} and Zr^{4+} after ageing at 1000 °C, Ce^{4+} (0.097 nm) and Zr^{4+} (0.084 nm) with small ionic radius entering into the oxide lattice of Nd^{3+} (0.115 nm) with larger ionic radius, leading to a larger unit cell parameters. In previous study [14], it is also found that there is no pure tetragonal phase after heat treatment at 1170 °C in the ZrO_2–Nd_2O_3 system with Nd contents more than 15 mol%. As shown in Table 1, the crystalline size of all aged samples is an increase comparing to the fresh samples, proving that the samples appear sintering, which induces the shrinkage of lattice parameters of CeO_2–ZrO_2. This is agreement with the literature [15]. CZN2A has the smallest crystalline size of 10.8 nm, while CZN5A has the largest crystalline size of 12.4 nm, indicating that phase transition can affect the crystalline size of the material. Suitable doping content can maintain the nanometer crystalline with CeO_2–ZrO_2 cubic phase, which would favor the active component dispersion of catalysts.

Since there are two competing effects on the peak-shift in XRD with different Nd doping concentrations, including contraction by the replacement of Ce^{4+} with Zr^{4+} and expansion by the increased fraction of Nd^{3+} or more oxygen vacancies. In order to study the oxygen vacancies of Nd doped materials, the lattice strain was calculated from the diffraction peaks of XRD. According to the literature [16,17], the lattice strain mainly comprises of non stoichiometric oxygen defects and Ce^{3+} (as Ce_2O_3) in CeO_2. These

Table 1
The lattice strain, crystalline cell parameter and size of $Ce_{0.35}Zr_{0.65-x}Nd_xO_{2-x/2}$ calcined at 600 and 1000 °C.

Samples	Lattice strain		Lattice parameters (nm)		Crystalline size (nm)	
	600 °C	1000 °C	600 °C	1000 °C	600 °C	1000 °C
CeO_2	–	–	0.54112	0.54105	8.4	117.4
CZN1	0.0337	0.0160	0.52667	0.52446	5.1	11.6
CZN2	0.0438	0.0164	0.52885	0.52678	4.4	10.8
CZN3	0.0379	0.0151	0.53063	0.52811	4.7	11.4
CZN4	0.0247	0.0136	0.53360	0.52961	4.3	11.4
CZN5	0.0227	0.0107	0.53557	0.53245	4.5	12.4

defects increase the width of the diffraction peak (Fig. 1). The magnitude of strain is determined using Williamson–Hall (W–H) plot [16] and the corresponding data are listed in Table 1. It is found that Nd doping into CeO_2–ZrO_2 changes the lattice strain, which is due to oxygen vacancies and Ce^{3+} [16]. For all fresh samples, they have higher lattice strain value than the corresponding aged samples, meaning more oxygen vacancies and Ce^{3+} in fresh samples. Furthermore, 10 mol% Nd doping into CeO_2–ZrO_2 has the highest value with 0.0438 lattice strain compared to other samples, and after ageing at 1000 °C for 5 h, it still has the highest value, indicating that 10 mol% doping could be an optimal amount to oxygen vacancies. Increase of lattice strain is the result of the substitution effect of slightly larger Nd^{3+} (0.115 nm) on Ce^{4+} (0.097 nm), which is due to that trivalent Nd doping produces oxygen vacancies in the lattice to maintain charge balance. With the increase of Nd doping content, the lattice strain decreases but expands the lattice (Table 1). The lattice tries to minimize the strain by undergoing expansion, meaning that excessive doping content is not conducive to the production of oxygen vacancies. This may be related with Ce^{4+} (0.097 nm), Zr^{4+} (0.084 nm) and Nd^{3+} (0.115 nm) ion radius. After ageing, the lattice strain values decrease, implying that the concentrations of oxygen vacancies and Ce^{3+} ions decrease. This is because the diffusion of oxygen vacancies from the bulk to the surface becomes more difficult because of severe sintering, which is possibly limited by phase domain, grain boundary and textural properties [17]. Some of the doped Nd^{3+} will replace the core Ce^{4+} site, and some of the Nd^{3+} ions will sit on the surface. This is because small semiconductor nanocrystallites have the tendency of self purification, and the excess numbers of dopants are expelled from interior by self purification process [17]. In this process, these excess Nd^{3+} ions, on the surface and in the core, result in phase separation (CZN4A) and phase transformation (CZN5A) to prevent the growth of the nanocrystallites.

For pure CeO_2, a Raman peak at about 465 cm^{-1} is observed in Fig. 2, which is related to the F_{2g} mode [18]. This mode corresponds to symmetric breathing mode of the oxygen ions around each Ce^{4+} cation [19]. A metastable phase (t″) of $Ce_{1-x}Zr_xO_2$ with $x = 0.2$–0.6 lies at ca. 138, 312, 470–473, and 620 cm^{-1} [20]. Six characteristic lines of tetragonal D_{4h}^{15} ZrO_2 are located at 148, 264, 323, 467, 610 and 645 cm^{-1} [21], and Raman shifts at 187, 332, 391, 433, 538 and 1000 cm^{-1} belong to Nd_2O_3 [22]. In our previous study [8], it is found that $Ce_{0.35}Zr_{0.65}O_2$ has one strong Raman peak at 471 cm^{-1} with a weak peak at 627 cm^{-1}. The former is due to F_{2g} mode of *c*-CeO_2, and the latter is attributed to the presence of a defective structure in the CeO_2–ZrO_2 materials. The Raman spectra of the prepared materials are illustrated in Fig. 2. It is found that the strong Raman peak for CZN1F and CZN3F is observed at around 470 cm^{-1}, and shifts to 475 cm^{-1} for CZN2F and CZN4F and to 468 cm^{-1} for CZN5F. Shifting and broadening of the F_{2g} Raman peak of samples with the increase of Nd doping content indicate the local structure distortion, which is due to lattice spacing and atomic geometry of ceria on more Nd doping. This may be caused by replacement of a lattice site Ce^{4+} with Nd^{3+}. All samples have two broad weak peaks at about 300 and 600 cm^{-1}. The strong

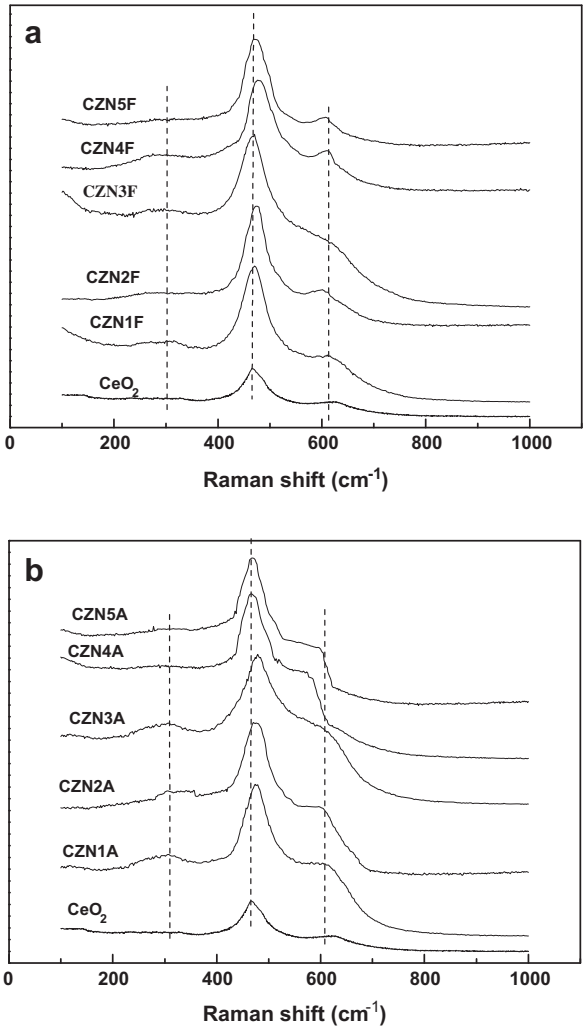

Fig. 2. The Raman spectra of all samples: (a) fresh samples and (b) aged samples.

Raman peak is due to the F_{2g} mode of *c*-CeO_2. For the weak peaks, the former at 300 cm^{-1} could be the t″ phase, and the latter belongs to the presence of a defective structure in the CeO_2–ZrO_2 materials [23]. This defect is attributed to the presence of intrinsic O vacancies in the lattice [24]. The t″ phase cannot be distinguished from the cubic phase by XRD since it is characterized by a cubic cation sub-lattice ($c/a = 1$), with tetragonal distortion of the oxygen sub-lattice [25]. After being aged at 1000 °C for 5 h, the strong Raman peaks of all samples has changed, indicating that there are rearrangement of Ce^{4+}, Zr^{4+} and Nd^{3+} and lattice shrinkage. All aged samples still maintain cubic phase. In XRD characterization, CZN4A takes place phase separation with cubic $Ce_{0.60}Nd_{0.40}O_{1.80}$ and cubic $Ce_{0.40}Zr_{0.60}O_2$, and CZN5A has a cubic $Nd_{0.50}Zr_{0.50}O_{1.75}$.

This indicates that Raman spectroscopy cannot clearly distinguish the difference of cubic phases containing ZrO_2 component but can describe oxygen vacancies and changes of ion position under our experimental conditions.

3.2. Textural properties and OSC of $Ce_{0.35}Zr_{0.65-x}Nd_xO_{2-x/2}$

The differences in the texture can be also seen in the parameters of porous structure calculated from the nitrogen adsorption isotherms collected in Table 2. All samples calcined at 600 °C have larger surface area, and the BET surface area and pore volume of CZN3F reach a maximum, 97 m^2/g and 0.19 ml/g. The former will favor the dispersion of active ingredients, and the latter is related to the diffusion of reactive molecules. After being aged at 1000 °C for 5 h, all samples undergo a loss of surface area, indicating that $Ce_{0.35}Zr_{0.65-x}Nd_xO_2$ could appear some complicated rearrangement of ions and sample sintering under high temperature. CZN3A still has 33 m^2/g of surface area and 0.13 cm^3/g of pore volume, indicating that suitable Nd doping can enhance the thermal stability of materials, which may improve the catalyst performance.

Table 2
The specific surface area (S_{BET}), pore volume (V) and oxygen storage capacity (OSC) of $Ce_{0.35}Zr_{0.65-x}Nd_xO_{2-x/2}$ calcined at 600 and 1000 °C.

Samples	S_{BET} (m^2/g)		V (ml/g)		OSC (μmol/g)	
	600 °C	1000 °C	600 °C	1000 °C	600 °C	1000 °C
CZN1	85	20	0.15	0.08	269	235
CZN2	86	26	0.16	0.08	416	292
CZN3	97	33	0.19	0.13	278	138
CZN4	85	35	0.15	0.12	237	124
CZN5	89	29	0.15	0.10	246	41

The OSC of $Ce_{0.35}Zr_{0.65-x}Nd_xO_{2-x/2}$ calcined at 600 and 1000 °C is listed in Table 2. All samples have different OSC. The OSC of CZN2F is 416 μmol/g, which is due to more oxygen vacancies. With the increase of Nd doping content, the OSC decreases, indicating that excessive Nd doping is not conducive to the enhancement of OSC because of the decrease of oxygen vacancies. Another factor is that the crystallite sizes of the fresh samples are small and large amount of crystal defects are created to increase the oxygen mobility both in the bulk and on the surface. The aged samples have similar tendency with the fresh samples and are closely related to oxygen vacancy content. Furthermore, the crystallite sizes of the aged samples are growth, and the crystal defects are decrease. They will reduce the oxygen mobility, resulting in the decrease of OSC. For CZN5A, the OSC decreases to 45 μmol/g. This may be due to the CeO_2–ZrO_2 transformation into Nd_2O_3–ZrO_2, indicating that $Ce^{3+} \leftrightarrow Ce^{4+}$ are the main ways of the oxygen storage.

3.3. Study of temperature-programmed reduction (TPR)

The reductive properties of the samples used in the present study are investigated using H_2-TPR to verify the doped effects of Nd_2O_3. The TPR profiles of fresh and aged $Ce_{0.35}Zr_{0.65-x}Nd_xO_{2-x/2}$ are illustrated in Fig. 3. Zhu et al. [26] have found that the reduction of CeO_2 starts at 280 °C, and the peak at 510 °C is assigned

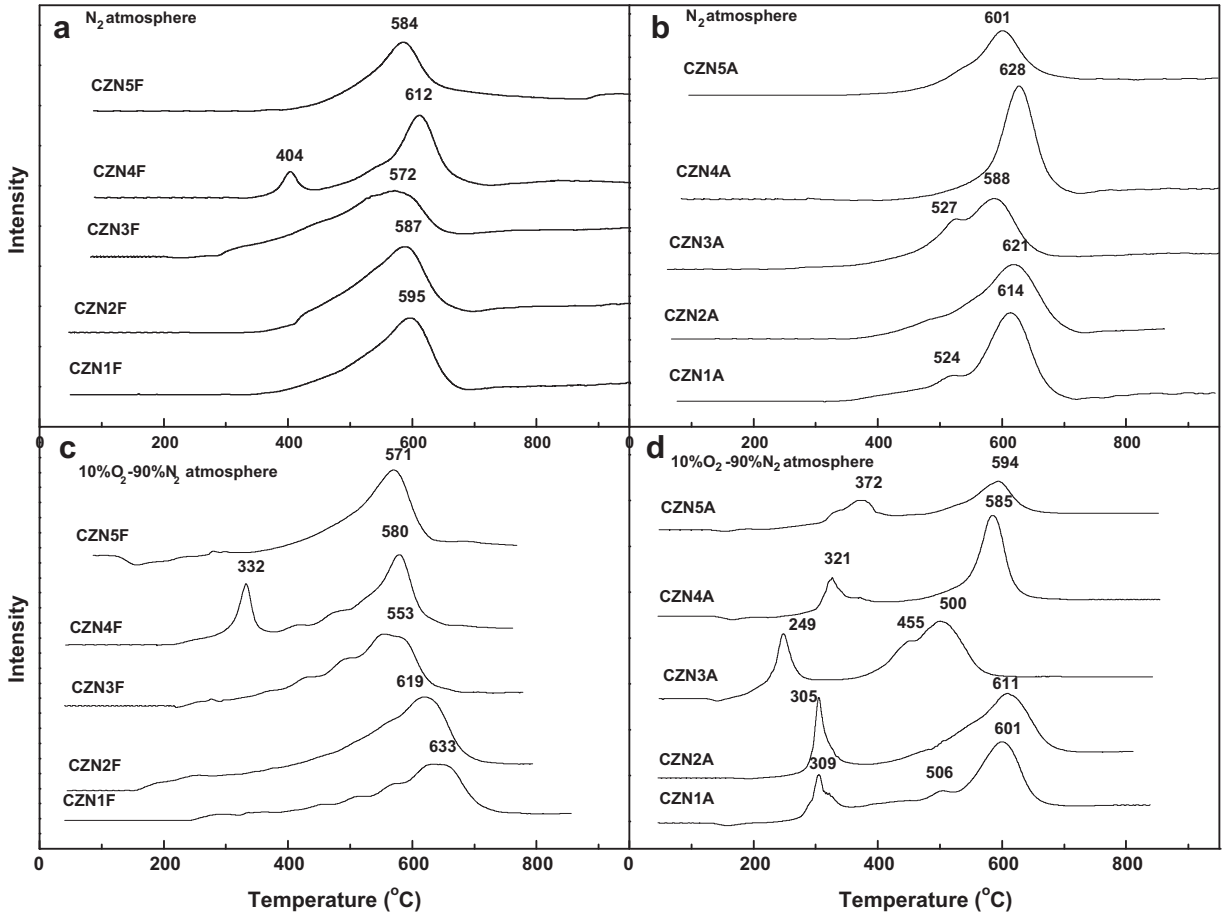

Fig. 3. The H_2-TPR of fresh (a) and aged (b) $Ce_{0.35}Zr_{0.65-x}Nd_xO_{2-x/2}$ after pretreatment under a N_2 atmosphere, and that of fresh (c) and aged (d) $Ce_{0.35}Zr_{0.65-x}Nd_xO_{2-x/2}$ after pretreatment under a 10%O_2–90%N_2 atmosphere.

to the reduction of surface capping oxygen of ceria, and the peak at 800 °C can be ascribed to the reduction of bulk CeO_2. Teng et al. [27] have reported that two reduction peaks (420 and 567 °C) of *m*-$Ce_{0.8}Zr_{0.2}O_2$ correspond to the reduction of oxygen from surface and bulk ceria, respectively. In Fig. 3a, the peak temperature shifts to lower temperature with the increase of Nd doping content, 595 °C for CZN1F, 587 °C for CZN2F and 572 °C for CZN3F, but for CZN4F, two reduction peaks are observed, 404 and 612 °C. The former is ascribed to the reduction of surface capping oxygen (O^{2-} and O^-) species due to the defects of structure and electronic properties of nonstoichiometric ceria [28], and the latter is assigned to surface cerium. This may be that the introduction of Nd^{3+} content has reached a critical point, resulting in a different TPR behavior. For CZN5F, the reduction peak towards to the low temperature at 584 °C. These results show that when different Nd doping contents are induced into CeO_2–ZrO_2, the oxygen mobility increases from bulk to surface. This may be due to the structural modification in the CeO_2–ZrO_2 lattice when some Ce^{4+} ions with small ionic radius are substituted by Nd^{3+} with large ionic radius. As reported in literatures [29,30], the introduction of Nd^{3+} in CeO_2–ZrO_2 lattice can induce structure disorder and create additional anion vacancies, which can increase the oxygen mobility in the bulk of solid solution, causing that partial O^{2-} anion diffuses from bulk to surface, resulting in the increase of the bulk reducibility. As shown in Table 3, CZN5F has the lowest H_2 consumption, indicating that cerium in CeO_2–ZrO_2 doped by high Nd^{3+} content is not easy reduced by hydrogen, which does not favor the oxygen mobility. This is consistent with the reported results in literature [31]. In Fig. 3b, compared to the reductive behavior of fresh samples, the peak temperatures of all aged samples shift to higher temperatures. Two reduction peaks for CZN1A are observed, 524 and 614 °C. Both CZN2A and CZN5A still have one reduction peak, but the peak temperature shifts to 621 and 601 °C, respectively. For CZN3A, a single reduction peak splits into two reduction peak, but one reduction peak for CZN4A is detected. On the one hand, there are a collapse of surface area and a filling of pore, which can hinder the concomitant reduction of the surface. Conversely, the different initial texture of the solid solution modifies the reduction temperatures in the TPR. On the other hand, the samples after ageing at 1000 °C appear different sintering and crystal growth. At the same time, the lattice shrinkage of $Ce_{0.35}Zr_{0.65-x}Nd_xO_{2-x/2}$ is observed of rearrangement of Ce, Zr and Nd ions. These factors influence the oxygen mobility, resulting in different reduction behavior. In Table 3, the H_2 consumption of all aged samples also changes obviously. Except CZN4A, the H_2 consumption of other samples decreases, proving that the reduction degree of Ce^{4+} in samples is reduced. CZN2A has the largest H_2 consumption, indicating that 10 mol% Nd content is conducive to the reduction of Ce^{4+} and the oxygen mobility. CZN5A has the worst H_2 consumption (191 μmol/g), which may be that Ce^{4+} ions enter into Nd_2O_3–ZrO_2 lattice and the interior Ce^{4+} is reduced difficultly.

Generally, there are several oxygen ad-species such as O_2^-, O_2^{2-}, and O^- on the surface of an oxygen-containing catalyst. Semiconductor oxides and some metal surface can adsorbed O_2 (including some O_2^-) at the lower temperature, while at higher temperatures, O_2 or O_2^- is dissociated into O^- and adsorbed on the oxide surface. The order of the adsorption energy of the three kinds of particles is $O_2 < O_2^- < O^-$. Yao and Yu Yao [32] also have found that a new oxygen species, probably a molecular oxygen anion, is formed at 25 °C which converts slowly at 500 °C to the capping oxygen anion, and complete restoration of all three types of oxygen anions is accomplished at 850 °C in air. In our work, when the fresh $Ce_{0.35}Zr_{0.65-x}Nd_xO_{2-x/2}$ is pretreated under a 10%O_2–90%N_2 atmosphere at 400 °C, as shown in Fig. 3c, the reductive behavior of the samples is similar to the samples pretreated by N_2, but the peak temperature shifts to low temperature except the peak of CZN1F at 633 °C and CZN2F at 619 °C, indicating that Ce^{4+} concentration on the surface occurs changes when $Ce_{0.35}Zr_{0.65-x}Nd_xO_{2-x/2}$ is pretreated under a 10%O_2–90%N_2 atmosphere. Oxygen vacancies in CZN1F and CZN2F decrease because non stoichiometric oxygen defects and Ce^{3+} (as Ce_2O_3) could be oxidized to Ce^{4+} after treatment under 10%O_2–90%N_2 atmosphere, resulting in reduction temperature to move to high temperature. In Table 3, H_2 consumption of CZN1F decreases to 204 μmol/g, which could be due to less defects because of low Nd^{3+} content. H_2 consumption of the others increases. This is because oxygen is absorbed on the surface of samples when the samples are oxidized at 400 °C. On the other hand, the more Nd^{3+} with larger ionic radius in CeO_2–ZrO_2 lattice can enhance defects, resulting in the increase of oxygen mobility. In Fig. 3d, three reductive peaks at 309, 506 and 601 °C are observed for CZN1A, corresponding to H_2 consumption of 26, 8 and 357 μmol/g, respectively. The former is due to the reduction of the absorbed oxygen, the medium is attributed to the reduction of surface-capping oxygen of ceria, and the latter belongs to the reduction of surface CeO_2. Except that the H_2 consumption of CZN5A is a decline compared to fresh samples, and that of the other samples increases, indicating that O_2 pretreatment can change the reduction behavior of samples. This is caused by lattice shrinkage because of rearrangement of Ce, Zr and Nd ions and a collapse of surface area after ageing at 1000 °C. When the aged samples were pretreated again in 10%O_2–90%N_2 atmosphere at 400 °C, all samples subjected to a secondary change of microenvironment, leading to a difference of reductive behavior and H_2 consumption compared to the samples treated by N_2. Especially, a reduction peak at low temperature is detected, which is due to the reduction of adsorbed oxygen species in the oxidation treatment. The increase of H_2 consumption is due to the reduction of adsorbed oxygen species and also includes the increase of the Ce^{4+} concentration on surface.

As shown in Fig. 4a, when noble metals are impregnated on the carriers, including $Ce_{0.35}Zr_{0.65-x}Nd_xO_{2-x/2}$ and La_2O_3-stabilized Al_2O_3, three reductive peaks are observed, showing that Pt-Rh/$Ce_{0.35}Zr_{0.65-x}Nd_xO_{2-x/2}$/$Al_2O_3$ has similar reduction behavior. In the study about the rhodium supported on ceria–zirconia mixed oxides, Haneda et al. [33] observed a reductive peak at 100 °C that was ascribed mainly to the reduction of nearby CeO_2–ZrO_2, which strongly interacts with rhodium. Fornasiero et al. [34] studied the interaction of molecular hydrogen with a Pt/$Ce_{0.6}Zr_{0.4}O_2$/Al_2O_3 TWC and observed an intense peak at 180 °C in the fresh sample, which was associated with the reduction of the Pt oxide and $Ce_{0.6}Zr_{0.4}O_2$ mixed oxide. In our previous work [35], the reduction peak at 104 °C of fresh Pt–Rh/CeO_2–ZrO_2–M_xO_y (M = Y, La)/Al_2O_3 is assigned to Rh, at 170 °C for Pt, and at 436 °C for Ce^{4+}. Thus, for example, both peaks at 198 and 239 °C are found during the TPR of C1F. The former may be associated with the reduction of Rh_2O_3 because of the formation of Rh_2O_3 in calcination process under oxidizing atmosphere [36], which can simultaneously involve the reduction of superficial cerium oxide, and the latter is due to the reduction of the Pt oxide and CZN1F mixed oxide. This is caused by strong

Table 3
The H_2 consumption of fresh (a) and aged (b) $Ce_{0.35}Zr_{0.65-x}Nd_xO_{2-x/2}$ pretreated under N_2 atmosphere after pretreatment under a N_2 atmosphere, and that of fresh (c) and aged (d) $Ce_{0.35}Zr_{0.65-x}Nd_xO_{2-x/2}$ after pretreatment under a 10%O_2–90%N_2 atmosphere.

Sample	H_2 consumption (μmol/g)			
	a	*b*	*c*	*d*
CZN1	353	282	204	26, 8, 357
CZN2	442	320	504	106, 464
CZN3	424	105, 155	524	164, 179, 350
CZN4	28, 258	311	30, 286	56, 444
CZN5	246	191	356	74, 224

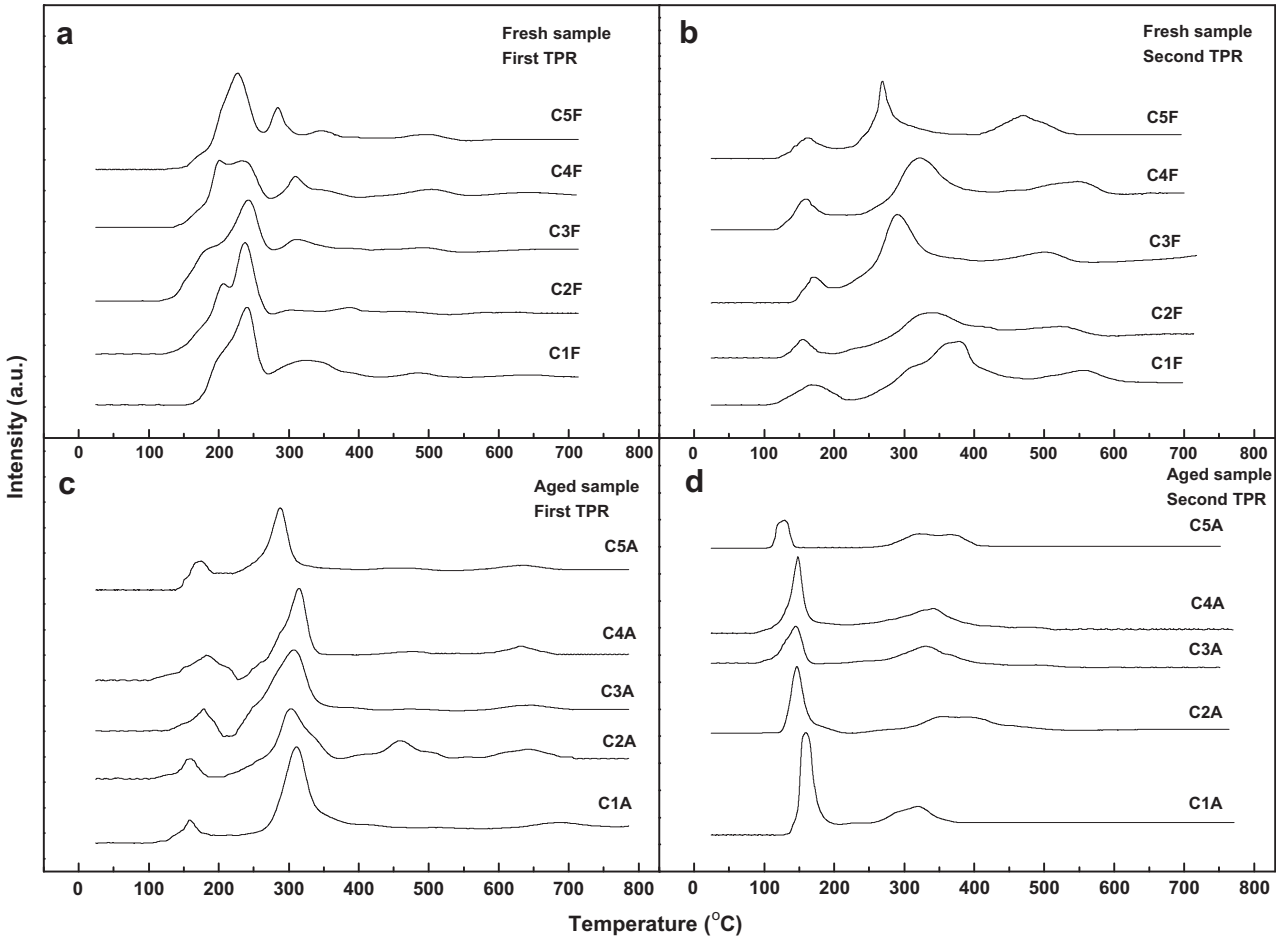

Fig. 4. The H_2-TPR of fresh (first (a) and second (b) cycle) and aged (first (c) and second (d) cycle) catalysts.

interaction between noble metal and $Ce_{0.35}Zr_{0.65-x}Nd_xO_{2-x/2}$. The noble metals have the capacity to anticipate cerium oxide reduction due to H_2 spillover from the metal to the CZN1F support, facilitating its reduction [37] which leads to the reduction of oxygen storage materials in catalysts shifting to low temperature (at around 327 °C) compared to $Ce_{0.35}Zr_{0.65-x}Nd_xO_{2-x/2}$. For the other catalyst samples, the reductive peaks appear slightly changes, indicating that Nd doping with different contents slightly influences reductive performance of catalysts because the differences of textures and crystalline size are resultant in different dispersion of noble metals. For the second TPR cycle of fresh catalysts, there are still three reductive peaks, but their reduction temperatures shift to higher temperatures, indicating that the catalysts undergo an ageing in the first cycle under H_2/N_2 atmosphere. The low temperature peak is due to the reduction of Rh_2O_3 and Pt oxides, the medium belongs to the reduction of noble metal involving cerium oxide, and the high is assigned to Ce^{4+} oxides. In impregnation process, carrier has different adsorption ability for active components, leading to competition adsorption, which will influence the distribution of active components on the carrier surface. On the other hand, the migration of impregnation liquid contained in pores will happen in drying process because of capillary phenomenon, which is resultant in uneven distribution of active components, forming uniform, egg-shell, egg-white and egg-yolk. The active ingredient encapsulated by carriers is exposed and starts to move and sinter in the H_2/N_2 atmosphere at high temperature [36]. When this process reaches a certain level, the catalyst will gradually deactivate and is an irreversible inactivation.

After ageing at 1000 °C, gray color of the catalyst surface is observed, indicating that noble metals (platinum and rhodium) are agglomerated because platinum and rhodium are certainly in the metallic state [38]. The reductive behavior of all samples has also undergone significant changes. Except that C2A has four obvious peaks, all other catalysts have two obvious reduction peaks at 100–200 and 200–350 °C and a broad peak at about 650 °C. The low temperature peak is due to the reduction of Rh_2O_3 and Pt oxides, the medium belongs to noble metal involving the reduction of Ce^{4+} oxides, and the latter is due to the bulk reduction of Ce^{4+} oxides. This may be that noble metal and carrier may sinter after ageing at 1000 °C resulting in the movement of reduction to high temperature. For C2A, the reduction peak at about 450 °C, which is due to a strong interaction between noble metals and carriers, resulting in a good anti-aging ability which will help to extend the service life of the catalyst. For the second TPR cycle of aged catalysts, all samples have two obvious reductive peaks. The peak below 200 °C becomes very sharp, and the reductive peak in the range of 300–400 °C becomes very small, indicating that grain growth of noble metals is accelerated in reducing atmosphere. The former still belongs to the reduction of noble metals, and the latter involves cerium oxide reduction. These results suggest that the noble metals in the carriers are slowly exposed and agglomerated, indicating that the catalyst inactivation is a slow process. Based on the above analysis, one can conclude that noble metals can influence the reductive behavior of $Ce_{0.35}Zr_{0.65-x}Nd_xO_{2-x/2}$, and $Ce_{0.35}Zr_{0.65-x}Nd_xO_{2-x/2}$ with different Nd doping content can change the sintering state of noble metals because of the thermal

stability of carrier materials, which will lead to the difference of three-way catalytic activities.

3.4. NO temperature-programmed desorption (NO-TPD) of catalysts

Several investigations have shown that NO_x can be stored on an alkaline-earth oxide (such as BaO) under excessive oxygen conditions, and the stored NO_x is then released and simultaneously reduced by CO or HC over the noble metal component [39,40] during intermittent rich/stoichiometric periods. However, the influence of Nd doping into CeO_2–ZrO_2 on NO_x removal for TWCs with low Pt and Rh is not investigated. As shown in Fig. 5, two desorption peaks of all catalysts are observed, indicating that catalysts have similar NO_x absorption behavior. For C1F, two desorption peaks of NO_x at 288 and 551 °C are observed. The former is due to the decomposition of species weakly adsorbed nitrite and NO, and the latter is caused by the decomposition of species strongly adsorbed nitrate (NO_3^-) species. This is because NO can be reacted with O_2 at lower temperature and generates NO_2. This NO_2 plays a role of surface oxidative agent to form NO_2–O_2^- pair; on the other hand, it can react with surface O to form a surface nitrate [29]. The area of peak at high temperature from larger to small is as follows: C4F > C2F > C3F > C5F > C1F. In TWCs, NO can be adsorbed on the ceria–zirconia and oxidized to NO_2, and this NO_2 is subsequently adsorbed as NO_3^- species on Ce^{4+}–O^{2-} pair sites [41], involving oxygen vacancies. This increase of activity is attributed to the ability of Ce^{3+}, generated by the metal-promoted reduction of the support, and to efficiently reduce NO via a redox mechanism. Both ad-NO_3^- species and adsorbed NO_2 species are important for NO reduction, because NO is oxidized to NO_2 under lean burn conditions and the resulting NO_2 can be absorbed as NO_3^-, which are periodically reduced by hydrocarbons [42]. Studies by Broqvist et al. [43] have shown that NO_2 is active species which can react with reducing gas and generates N_2. Therefore, the area of peak at high temperature is larger, and the generation of NO_3^- is more, which will influence the removal of NO_x under lean burn conditions.

3.5. Catalytic testing

The three-way catalytic activities of all catalysts under a simulated exhaust mixed gas and at SV = 34,000 h^{-1} are illustrated in Fig. 6. The conversions of CO, C_3H_8 and NO of all catalysts increase with the increasing temperatures. When the temperature rises to a certain value, the three pollutants may be completely converted. The light-off temperatures $T_{50\%}$ (the conversion reaches 50% corresponding to the reaction temperature) of all catalysts are listed in Table 4. The temperature of CO catalytic oxidation is the lowest, showing that CO is the most easily removed because CO is easily adsorbed on the catalyst surface and firstly be oxidized by mobile oxygen species on the catalyst surface. C_3H_8 is converted into CO_2 and H_2O, which needs higher temperature because of the dissociative chemisorption of C_3H_8 related to C–H band broken which is very difficult. NO conversion differs from HC conversion in having two mechanism routes: one is metal-catalyzed, and the other is oxygen-storage related and involves synergy between ceria–zirconia-based oxides and noble metals. CeO_2–ZrO_2-based materials could supply reactive oxygen by storage/release oxygen through a redox process involving the $Ce^{4+} \leftrightarrow Ce^{3+}$ couple, which can facilitate the oxygen adsorption and activation, and thus promotes the catalytic reactivity [44]. The noble metals facilitate the reduction of Ce^{4+}–Ce^{3+} (Fig. 4a), which can be oxidized by NO_x or O_2. On the other hand, the cerium component of CeO_2–ZrO_2-based oxides can capture oxygen from H_2O and produce CeO_2 and H_2 [45]. This promotes the removal of CO, C_3H_8 and NO, because CO and C_3H_8 involve water–gas shift and stream reforming [35], releasing hydrogen which is a very effective reductant for removing NO [45]. In Table 4, the light-off temperature ($T_{50\%}$) of C2F can be as low as 160 °C for CO, 211 °C for NO and 259 °C for C_3H_8, while that of C1F is 289 °C for C_3H_8, 242 °C for CO and 278 °C for NO. The catalytic activity of CO and C_3H_8 over catalysts from excellent to poor followed a sequence of C2F > C3F > C4F > C5F > C1F, which is closely related to the dispersion of noble metals and OSC. The former provides the active site, and the latter involves the movement of oxygen. In other words, oxygen storage materials must have high OSC and oxygen mobility, whereas a high surface area and appropriate pore structure mainly provide active sites. As shown in Table 4, the dispersion of C2F is 21.26%, which corresponds to best catalytic activity. The dispersion of C3F is 17.63%, and that of C4F and C5F is 14.56% and 13.28%, respectively. The C1F is only 7.26%, which corresponds to the worst catalytic activity. This is consistent with crystalline size of $Ce_{0.35}Zr_{0.65-x}Nd_xO_{2-x/2}$, indicating that small crystalline size favors the dispersion of the active component. It is confirmed that the performance of carrier, especially applications of oxygen storage materials, directly influences the catalytic activity of catalysts, because the removal of CO and C_3H_8 mainly depends on oxidation reaction [46]. The catalytic activity of NO over catalysts from poor to excellent followed a sequence of C1F < C5F < C3F < C2F < C4F, which is consistent with the results of NO_3^-, indicating that NO_2 is very important because it can be reduced by reducing agent, including hydrocarbons, CO and H_2.

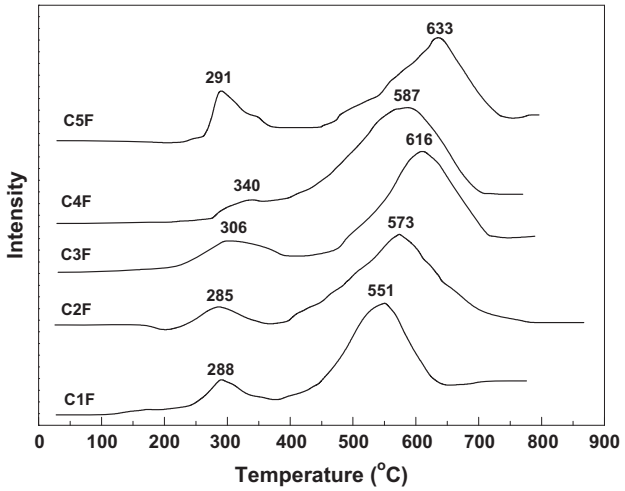

Fig. 5. NO-TPD of catalysts.

The CO, C_3H_8 and NO conversions of catalysts at 320 °C under different λ values are illustrated in Fig. 7. The λ width (W) values act as another scale for evaluating catalysts and are listed in Table 4, when CO, C_3H_8 and NO conversions all reach 80%, respectively. These data can be used to describe the three-way working window of catalysts and removal of pollutants under rich/lean burn conditions. In Fig. 7, in λ testing range, at $\lambda < 1$, CO could be almost completely converted into CO_2 because $Ce_{0.35}Zr_{0.65-x}Nd_xO_{2-x/2}$ can release oxygen; at $\lambda > 1$, NO conversion rapidly decreases; at $\lambda = 1$, C_3H_8 conversion almost goes to complete conversion. It must enhance C_3H_8 conversion at $\lambda < 1$ and NO conversion at $\lambda > 1$ to expand working-window of catalysts. The oxygen storage materials should satisfy two factors, including a wide operation range for redox $Ce^{3+} \leftrightarrow Ce^{4+}$ in reducing and oxidizing atmospheres and high reaction active sites. Oxygen storage material is used as a crucial component in TWCs, which could influence the dispersion of noble metals and the distribution of active sites as well as oxygen transfer. The working-window of

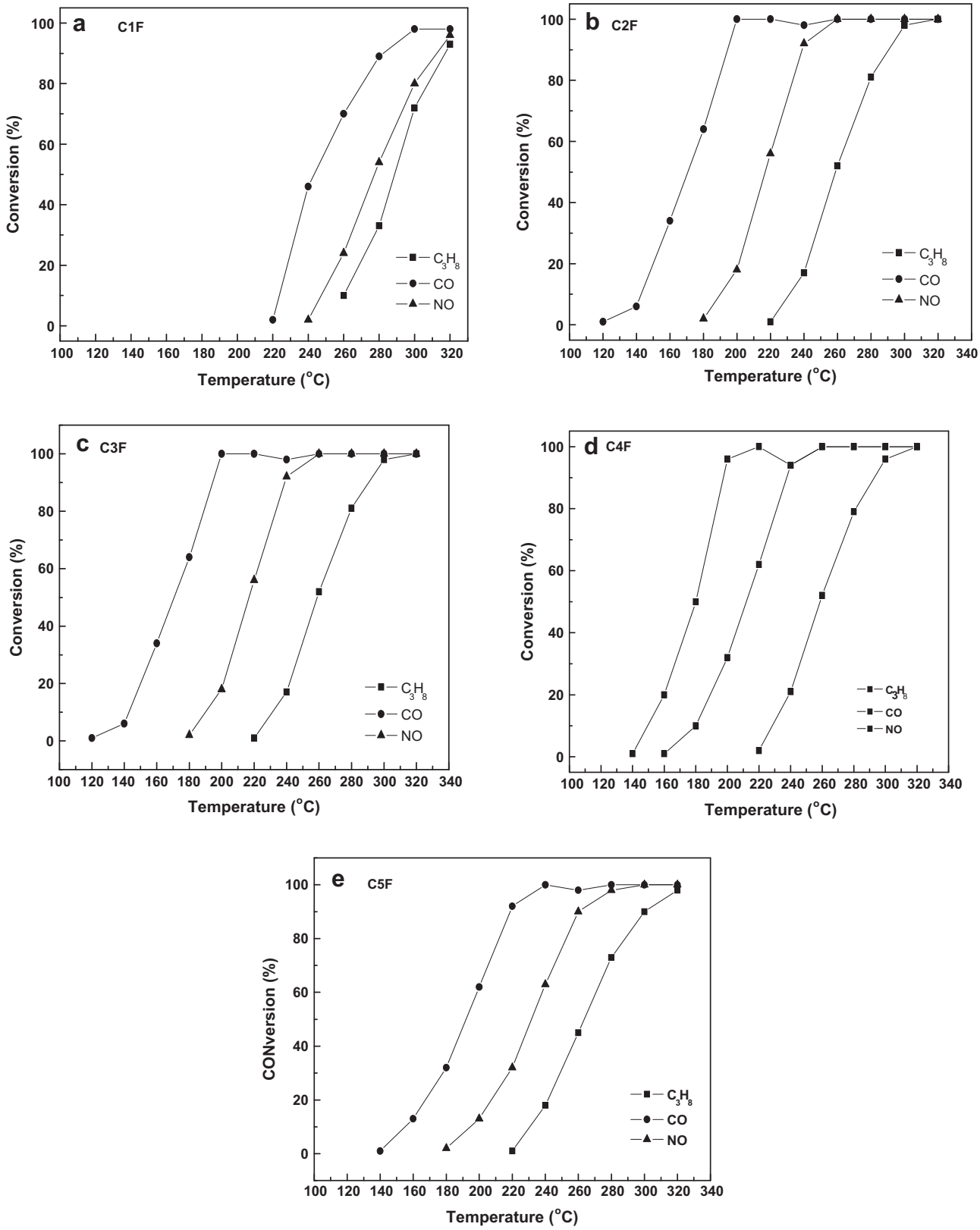

Fig. 6. The light-off temperature curves of catalysts.

catalysts from wide to narrow is as follows: C2F > C3F > C4F > C5F > C1F (Table 4). The C2F has the widest working-window, which is due to high oxygen vacancies, because oxygen can be absorbed on the oxygen vacancies and forms chemically adsorbed oxygen (O_2^-) [47]. This chemical adsorption can make O–O band weaken and form active O^- ions [48]. The "ionic" oxygen is active in total oxidation [49], which can improve CO and C_3H_8 oxidation. C_3H_8 oxidation influences the range of working-window

Table 4
The $T_{50\%}$ of C_3H_8, CO and NO over catalysts, working-window (W) and Pt and Rh dispersion.

Catalysts	$T_{50\%}$ (°C)			W	Pt and Rh dispersion (%)
	C_3H_8	CO	NO		
C1F	289	242	278	0.05	7.26
C2F	259	160	211	0.27	21.26
C3F	259	170	217	0.26	17.63
C4F	258	179	240	0.21	14.56
C5F	262	191	231	0.15	13.28

at $\lambda < 1$, because C_3H_8 oxidation needs sufficient active oxygen. If active oxygen cannot satisfy oxidation reaction, C_3H_8 conversion obviously decreases, resulting in a narrower working-window of catalysts. NO reduction influences the range of working-window at $\lambda > 1$, because NO is firstly oxidized to NO_2 under lean burn conditions and the resulting NO_2 can be absorbed as NO_3^-, which are periodically reduced by reducing agent, including HC, CO or H_2, during intermittent rich/stoichiometric periods. On the other hand, C2F has noble metal dispersion of 21.26%, which can provide more active sites. For C1F, it has the narrowest working-window, which is due to lower oxygen vacancies and low noble metal dispersion of 7.26%. This indicates that the properties of oxygen storage

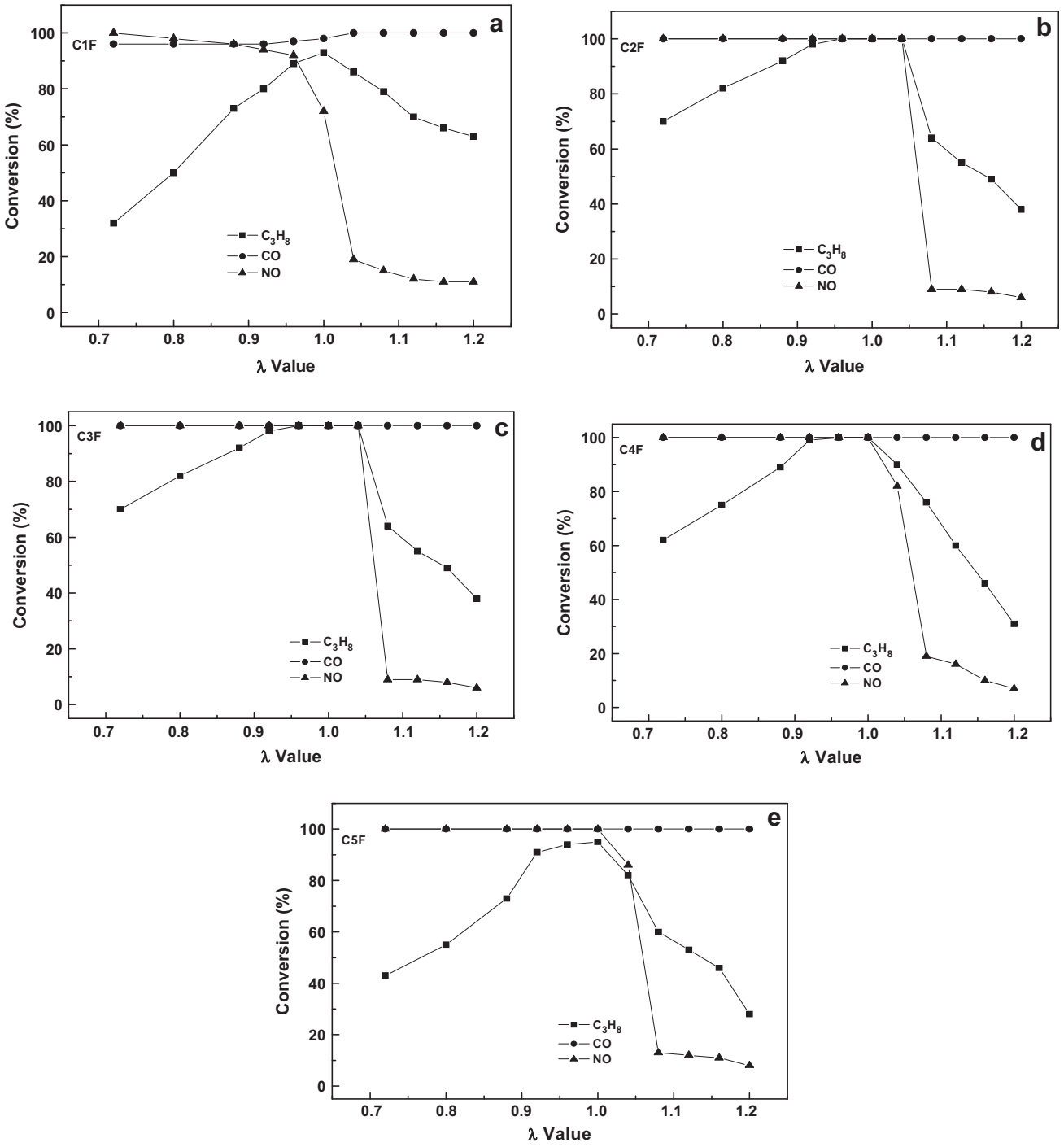

Fig. 7. The λ-cycling properties of catalysts.

materials and noble metal dispersion are very important for catalytic activities.

4. Conclusions

In the case of same Ce content, the doped Nd with different content significantly affects the textural and structural performance of $Ce_xZr_{0.65-x}Nd_xO_{2-x/2}$ as well as crystalline size. The $Ce_{0.35}Zr_{0.50}Nd_{0.10}O_{1.85}$ (CZN2) has more oxygen vacancy and corresponds to higher oxygen storage capacity (OSC), but excessive Nd doping is not conducive to the oxygen mobility of CeO_2–ZrO_2. All fresh samples show a cubic CeO_2–ZrO_2 with nano-size, but after ageing at 1000 °C, small $Ce_{0.60}Nd_{0.40}O_{1.80}$ is segregated from cubic $Ce_{0.40}Zr_{0.60}O_2$ for $Ce_{0.35}Zr_{0.45}Nd_{0.20}O_{1.90}$ (CZN4A) and the cubic $Ce_{0.40}Zr_{0.60}O_2$ phase completely converts into cubic $Nd_{0.50}Zr_{0.50}O_{1.75}$ phase for $Ce_{0.35}Zr_{0.40}Nd_{0.25}O_{1.875}$ (CZN5A), accompanying a sharp decline of the OSC. $Ce_{0.35}Zr_{0.65-x}Nd_xO_{2-x/2}$ shows important differences in the TPR and H_2 consumption and can change the dispersion and sintering of noble metals, resulting in different catalytic activities. The catalyst containing $Ce_{0.35}Zr_{0.55}Nd_{0.10}O_{1.95}$ (CZN2) exhibits best catalytic activities, indicating that the properties of oxygen storage materials are very important for catalyst activities. The suitable Nd doping content can better maintain the reductive properties, which beneficially improve catalysts to adapt to the working conditions of vehicle exhaust emissions under the operating conditions of the different working conditions.

Acknowledgements

This project is financially supported by the National Natural Science Found of China (21173153). We would like to thank the Sichuan University Analytical and Testing Center for the characterization of the catalyst.

References

[1] Sung, Catalyst composition for purifying exhaust gas, US 6492297, 2002.
[2] R. Huang, J. Li, R.G. Hurley, Low-precious metal/high-rare earth oxide catalysts, US 6540968, 2003.
[3] Y. Madier, C. Descorme, A.M. Le Govic, D. Duprez, Oxygen mobility in CeO_2 and $Ce_xZr(1-x)O_2$ compounds: study by CO transient oxidation and 18O/16O isotopic exchange, J. Phys. Chem. B 103 (1999) 10999–11006.
[4] L.N. Ikryyannikova, A.A. Aksenov, G.L. Markaryan, G.P. Muravieva, B.G. Kostyuk, A.N. Kharlanov, E.V. Lunina, The redox treatments influence on the structure and properties of M_2O_3–CeO_2–ZrO_2 (M=Y, La) solid solutions, Appl. Catal., A 210 (2010) 225–235.
[5] J.X. Guo, D.D. Wu, L. Zhang, M.C. Gong, M. Zhao, Y.Q. Chen, Preparation of nanometric CeO_2–ZrO_2–Nd_2O_3 solid solution and its catalytic performances, J. Alloys Comp. 460 (2008) 485–490.
[6] Q.Y. Wang, G.F. Li, B. Zhao, R.X. Zhou, The effect of Nd on the properties of ceria–zirconia solid solution and the catalytic performance of its supported Pd-only three-way catalyst for gasoline engine exhaust reduction, J. Hazard. Mater. 189 (2011) 150–157.
[7] W.T. Wallace, B.K. Min, D.W. Goodman, The nucleation, growth, and stability of oxide-supported metal clusters, Top. Catal. 34 (2005) 17–30.
[8] J.X. Guo, Z.H. Shi, D.D. Wu, H.Q. Yin, M.C. Gong, Y.Q. Chen, A comparative study of SrO and BaO doping to CeO_2–ZrO_2: characteristic and its catalytic performance for three-way catalysts, Mater. Res. Bull. 48 (2013) 495–503.
[9] V. Perrichona, L. Retailleaua, P. Bazinb, M. Daturib, J.C. Lavalley, Metal dispersion of CeO_2–ZrO_2 supported platinum catalysts measured by H_2 or CO chemisorption, Appl. Catal., A 260 (2004) 1–8.
[10] M. Yashima, T. Wakitak, Atomic displacement parameters and structural disorder of oxygen ions in the $Ce_xZr_{1-x}O_2$ solid solutions ($0.12 \leqslant x \leqslant 1.0$): possible factors of high catalytic activity of ceria–zirconia catalysts, Appl. Phys. Lett. 94 (2009) 171902–171902-3.
[11] D. Tan, G. Lin, Y. Liu, Y. Teng, Y. Zhuang, B. Zhu, Q. Zhao, J. Qiu, Synthesis of nanocrystalline cubic zirconia using femtosecond laser ablation, J. Nanopart. Res. 13 (2011) 1183–1190.
[12] S.V. Chavan, P.U.M. Sastry, A.K. Tyagi, Combustion synthesis of nano-crystalline Nd-doped ceria and Nd_2O_3 and their fractal behavior as studied by small angle X-ray scattering, J. Alloys Comp. 456 (2008) 51–56.
[13] D. Horlait, L. Claparède, N. Clavier, S. Szenknect, N. Dacheux, J. Ravaux, R. Podor, Stability and structural evolution of $Ce^{IV}_{1-x}Ln^{III}_xO_{2-x/2}$ solid solutions: a coupled μ-Raman/XRD approach, Inorg. Chem. 50 (2011) 7150–7161.
[14] E.R. Andrievskaya, L.M. Lopato, Influence of composition on the T → M transformation in the systems ZrO_2–Ln_2O_3 (Ln = La, Nd, Sm, Eu), J. Mater. Sci. 30 (1995) 2591–2596.
[15] F. Zhang, S.W. Chan, J.E. Spanier, E. Apak, Q. Jin, R.D. Robinson, I.P. Herman, Cerium oxide nanoparticles: size-selective formation and structure analysis, Appl. Phys. Lett. 80 (2002) 127–129.
[16] B. Choudhury, A. Choudhury, Ce^{3+} and oxygen vacancy mediated tuning of structural and optical properties of CeO_2 nanoparticles, Mater. Chem. Phys. 131 (2012) 666–671.
[17] B. Choudhury, A. Choudhury, Lattice distortion and corresponding changes in optical properties of CeO_2 nanoparticles on Nd doping, Curr. Appl. Phys. 13 (2013) 217–223.
[18] G.M. Dalpianand, J.R. Chelikowsky, Self-purification in semiconductor nanocrystals, Phys. Rev. Lett. 96 (2006) 226802.
[19] G. Vlaic, R.D. Monte, P. Fornasiero, E. Fonda, J. Kašpar, M. Graziani, Redox property–local structure relationships in the Rh-loaded CeO_2–ZrO_2 mixed oxides, J. Catal. 182 (1999) 378–389.
[20] M. Yashima, H. Arashi, M. Kakihana, M. Yoshimura, Raman scattering study of cubic–tetragonal phase transition in $Zr_{1-x}Ce_xO_2$ solid solution, J. Am. Ceramic Soc. 77 (1994) 1067–1071.
[21] X. Wu, X. Wu, Q. Liang, J. Fan, D. Weng, Z. Xie, S. Wei, Structure and oxygen storage capacity of Pr/Nd doped CeO_2–ZrO_2 mixed oxides, Solid State Sci. 9 (2007) 636–643.
[22] M. Widerøe, H. Fjellvåg, T. Norby, F.W. Poulsen, R.W. Berg, NdHO, a novel oxyhydroxide, J. Solid State Chem. 184 (2011) 1890–1894.
[23] R. Kostic, S. Askrabic, Z.D. Mitrovic, Z.V. Popovic, Low-frequency Raman scattering from CeO_2 nanoparticles, Appl. Phys. A 90 (2008) 679–683.
[24] J.L. Ayastuy, A. Gurbani, M.P. González-Marcos, M.A. Gutiérrez-Ortiz, Selective CO oxidation in H_2 streams on $CuO/Ce_xZr_{1-x}O_2$ catalysts: correlation between activity and low temperature reducibility, Int. J. Hydrogen Energy 37 (2012) 1993–2006.
[25] C. Bozo, F. Gaillard, N. Guilhaume, Characterisation of ceria–zirconia solid solutions after hydrothermal ageing, Appl. Catal., A 220 (2001) 69–77.
[26] H. Zhu, Z. Qin, W. Shan, W. Shen, J. Wang, Pd/CeO_2–TiO_2 catalyst for CO oxidation at low temperature: a TPR study with H_2 and CO as reducing agents, J. Catal. 225 (2004) 267–277.
[27] M. Teng, L. Luo, X. Yang, Synthesis of mesoporous $Ce_{1-x}Zr_xO_2$ ($x = 0.2-0.5$) and catalytic properties of CuO based catalysts, Microporous Mesoporous Mater. 119 (2009) 158–164.
[28] C. Li, G. Zhou, L. Wang, S. Dong, J. Li, T. Cheng, Effect of ceria on the MgO–γ-Al_2O_3 supported $CeO_2/CuCl_2/KCl$ catalysts for ethane oxychlorination, Appl. Catal., A 400 (2011) 104–110.
[29] S. Yamazaki, T. Matsui, T. Ohashi, Y. Arita, Defect structures in doped CeO_2 studied by using XAFS spectrometry, Solid State Ionics 136–137 (2000) 913–920.
[30] J. Mikulova, S. Rossignol, F. Gerard, D. Mesnard, C. Kappenstein, D. Duprez, Properties of cerium–zirconium mixed oxides partially substituted by neodymium: comparison with Zr–Ce–Pr–O ternary oxides, J. Solid State Chem. 179 (2006) 2511–2520.
[31] R. Si, Y.W. Zhang, L.M. Wang, S.J. Li, B.X. Lin, W.S. Chu, Z.Y. Wu, C.H. Yan, Enhanced thermal stability and oxygen storage capacity for $Ce_xZr_{1-x}O_2$ ($x = 0.4-0.6$) solid solutions by hydrothermally homogenous doping of trivalent rare earths, J. Phys. Chem. C 111 (2006) 787–794.
[32] H.C. Yao, Y.F. Yu Yao, Ceria in automotive exhaust catalysts I. Oxygen storage, J. Catal. 86 (1984) 254–265.
[33] M. Haneda, K. Shinoda, A. Nagane, O. Houshito, H. Takagi, Y. Nakahara, K. Hiroe, T. Fujitane, H. Hamada, Catalytic performance of rhodium supported on ceria–zirconia mixed oxides for reduction of NO by propene, J. Catal. 259 (2008) 223–231.
[34] P. Fornasiero, J. Kašpar, T. Montini, M. Graziani, V. Dal Santo, R. Psaro, S. Recchia, Interaction of molecular hydrogen with three-way catalyst model of $Pt/Ce_{0.6}Zr_{0.4}O_2/Al_2O_3$ type, J. Mol. Catal. A 204-205 (2003) 683–691.
[35] J.X. Guo, S.H. Yuan, D.D. Wu, H.Q. Yin, M.C. Gong, Y.Q. Chen, Study of Pt–Rh/CeO_2–ZrO_2–MxOy (M = Y, La)/Al_2O_3 three-way catalysts, Appl. Surf. Sci. 273 (2013) 527–535.
[36] Z. Hu, F.M. Allen, C.Z. Wan, R.M. Heck, J.J. Steger, R.E. Lakis, C.E. Lyman, Performance and structure of Pt–Rh three-way catalysts: mechanism for Pt/Rh synergism, J. Catal. 174 (1998) 13–21.
[37] E. Rogemond, R. Frety, V. Perrichon, M. Primet, M. Chevrier, C. Gauthier, F. Mathis, Evolution of the ceria surface area of Pt–Rh ceria-alumina catalysts submitted to hydrothermal aging at 1273 K, Appl. Catal., A 156 (1997) 253–265.
[38] J.Z. Shyu, K. Otto, Characterization of Pt/γ-alumina catalysts containing ceria, J. Catal. 115 (1989) 16–23.
[39] N. Takahashi, H. Shinjoh, T. Iijima, T. Suzuki, K. Yamazaki, K. Yokota, H. Suzuki, N. Miyoshi, S. Matsumoto, T. Tanizawa, S. Tanaka, T. Tateishi, K. Kashara, The new concept 3-way catalyst for automotive lean-burn engine: NO_x storage and reduction catalyst, Catal. Today 27 (1996) 63–69.
[40] S. Matsumoto, Recent advances in automobile exhaust catalyst, Catal. Surv. Jpn. 1 (1997) 111–117.
[41] M. Haneda, T. Morita, Y. Nagao, Y. Kintaichia, H. Hamada, CeO_2–ZrO_2 binary oxides for removal by sorption NO_x, Phys. Chem. Chem. Phys. 3 (2001) 4696–4700.
[42] X. Wu, Q. Liang, D. Weng, J. Fan, R. Ran, Synthesis of CeO_2–MnO_x mixed oxides and catalytic performance under oxygen-rich condition, Catal. Today 126 (2007) 430–435.

[43] P. Broqvist, H. Grönbeck, I. Panas, E. Fridell, Characterization of NO_x species adsorbed on BaO: experiment and theory, J. Phys. Chem. B 108 (2004) 3523–3530.
[44] L. Wang, L.F. Zhang, S.L. Zhong, A.W. Xu, Highly uniform CeO_2 hierarchical microstructures: facile synthesis and catalytic activity evaluation, Appl. Surf. Sci. 263 (2012) 769–776.
[45] T. Bunluesin, R.J. Gorte, G.W. Graham, CO oxidation for the characterization of reducibility in oxygen storage components of three-way automotive catalysts, Appl. Catal. B 14 (1997) 105–115.
[46] P. Fornasiero, R. Di Monte, G. Ranga Rao, J. Kašpar, S. Meriani, A. Trovarelli, M. Graziani, Rh-loaded CeO_2–ZrO_2 solid-solutions as highly efficient oxygen exchangers: dependence of the reduction behavior and the oxygen storage capacity on the structural-properties, J. Catal. 151 (1995) 168–177.
[47] A. Martínez-Arias, M. Fernández-García, C. Belver, J.C. Conesa, J. Soria, EPR study on oxygen handling properties of ceria, zirconia and Zr–Ce (1:1) mixed oxide samples, Catal. Lett. 65 (2000) 197–204.
[48] M. Che, A.J. Tench, Characterization and reactivity of molecular oxygen species on oxide surfaces, Adv. Catal. 32 (1983) 1–148.
[49] V.I. Bukhtiyarov, I.P. Prosvirin, R.I. Kvon, Study of reactivity of oxygen states adsorbed at a silver surface towards C_2H_4 by XPS, TPD and TPR, Surf. Sci. 320 (1994) L47–L50.